



Published in final edited form as:

*Nat Commun.* ; 5: 5440. doi:10.1038/ncomms6440.

## A mononuclear nonheme iron(III)-superoxo complex: Crystallographic and spectroscopic characterization and reactivities

Seungwoo Hong<sup>1</sup>, Kyle D. Sutherlin<sup>2</sup>, Jiyoung Park<sup>1</sup>, Eunji Kwon<sup>1</sup>, Maxime A. Siegler<sup>3</sup>,  
Edward I. Solomon<sup>2,4,\*</sup>, and Wonwoo Nam<sup>1,\*</sup>

<sup>1</sup>Department of Chemistry and Nano Science, Ewha Womans University, Seoul 120-750, Korea

<sup>2</sup>Department of Chemistry, Stanford University, Stanford, CA 94305, USA

<sup>3</sup>Department of Chemistry, The Johns Hopkins University, Baltimore, Maryland 21218, USA

<sup>4</sup>Stanford Synchrotron Radiation Laboratory, Stanford Linear Accelerator Center, Menlo Park, CA 94025, USA

### Abstract

Mononuclear nonheme iron(III)-superoxo species ( $\text{Fe}^{\text{III}}\text{-O}_2^{\bullet-}$ ) have been implicated as key intermediates in the catalytic cycles of dioxygen activation by nonheme iron enzymes. Although nonheme iron(III)-superoxo species have been trapped and characterized spectroscopically in enzymatic and biomimetic reactions, no structural information has yet been obtained. Here we report for the first time the isolation, spectroscopic characterization, and crystal structure of a mononuclear side-on ( $\eta^2$ ) iron(III)-superoxo complex with a tetraamido macrocyclic ligand (TAML),  $[\text{Fe}^{\text{III}}(\text{TAML})(\text{O}_2)]^{2-}$  (**1**). The nonheme iron(III)-superoxo species undergoes both electrophilic and nucleophilic oxidation reactions as well as  $\text{O}_2$ -transfer between metal complexes. In the  $\text{O}_2$ -transfer reaction, **1** transfers the bound  $\text{O}_2$  unit to a manganese(III) analogue, resulting in the formation of a manganese(IV)-peroxo complex,  $[\text{Mn}^{\text{IV}}(\text{TAML})(\text{O}_2)]^{2-}$  (**2**); **2** is characterized structurally and spectroscopically as a mononuclear side-on ( $\eta^2$ ) manganese(IV)-peroxo complex. The difference in the redox distribution between the metal ions and  $\text{O}_2$  in **1** and **2** is rationalized using density functional theory calculations.

### Introduction

Metal-dioxygen adducts ( $\text{M-O}_2$ ), such as metal-superoxo and metal-peroxo species, are invoked as key intermediates in the transport, storage, and activation of dioxygen ( $\text{O}_2$ ) by

Reprints and permission information is available online at <http://npg.nature.com/reprintsandpermissions/>.

\*Correspondence and requests for materials should be addressed to Wonwoo Nam ([wynam@ewha.ac.kr](mailto:wynam@ewha.ac.kr)) and Edward I. Solomon ([edward.solomon@stanford.edu](mailto:edward.solomon@stanford.edu)).

#### Author contributions

W.N. and E.I.S. conceived and designed the experiments; S.H., K.D.S., J.P., and E.K. performed the experiments; S.H., K.D.S., and M.A.S. analysed the data; W.N., E.I.S., S.H., and K.D.S. co-wrote the paper.

#### Additional information

Supplementary information and chemical compound information accompany this paper at [www.nature.com/naturecommunications](http://www.nature.com/naturecommunications).

metal-containing proteins and enzymes as well as in O<sub>2</sub>-formation by Photosystem II<sup>1-4</sup>. The structures and spectroscopic properties of O<sub>2</sub>-binding metal complexes have been investigated intensively over the past half-century, and several crystal structures of O<sub>2</sub>-binding iron species have been reported in heme and nonheme iron enzymes and their model compounds<sup>5-10</sup>. One of the first reported crystal structures of an O<sub>2</sub>-bound iron intermediate was obtained using a synthetic heme complex as a model of oxy-hemoglobin and oxy-myoglobin<sup>8</sup>. The structural and spectroscopic characterization of the O<sub>2</sub>-binding iron intermediates in heme-containing proteins and synthetic iron porphyrins revealed that these iron(III)-superoxo species bind the O<sub>2</sub> unit in an end-on fashion<sup>7-9</sup>. In contrast, crystal structures of iron-O<sub>2</sub> intermediates in nonheme iron enzymes and models revealed that the O<sub>2</sub> unit in iron(III)-peroxo species binds to the iron center in a side-on fashion<sup>5, 6, 10</sup>; the crystal structure of a mononuclear nonheme iron(III)-peroxo complex, [Fe<sup>III</sup>(TMC)(O<sub>2</sub>)]<sup>+</sup>, TMC = 1,4,8,11-tetramethyl-1,4,8,11-tetraazacyclotetradecane), shows the binding of O<sub>2</sub> unit in a side-on fashion with an O-O bond distance of 1.463(6) Å<sup>10</sup>. Another example is the structure of naphthalene dioxygenase which shows an O<sub>2</sub> unit bound in a side-on fashion<sup>6</sup>. However, to the best of our knowledge, no structural information has been obtained for nonheme iron(III)-superoxo species, although such intermediates have been proposed under catalytic reaction conditions and trapped and characterized spectroscopically in nonheme iron enzymes and models<sup>11-13</sup>. For example, Nam and co-workers proposed the short-lived “putative” Fe(III)-superoxo intermediate during the dioxygen activation by nonheme iron(II) complexes while Goldberg and co-workers demonstrated that the binding sulfur ligand at the axial position iron(II) complex facilitated the O<sub>2</sub> binding, therefore, generating iron(III)-superoxo species. However, none of these showed direct structural evidence of the iron(III)-superoxo species.<sup>14-16</sup> Further, although nonheme iron(III)-superoxo intermediates have been proposed as reactive species in electrophilic oxidation reactions by nonheme iron complexes, direct evidence for the involvement of such nonheme iron(III)-superoxo species in electrophilic oxidation reactions has not been reported in nonheme iron models<sup>17, 18</sup>. Furthermore, the involvement of nonheme iron(III)-superoxo species in nucleophilic oxidation reactions has been rarely discussed in either enzymatic or biomimetic reactions. Thus, understanding the structural information and chemical properties, in particular the oxidation reactivity, of iron(III)-superoxo species has become an important objective for bioinorganic chemists.

We now report for the first time the synthesis, spectroscopic and electronic properties, and crystal structure of a mononuclear side-on ( $\eta^2$ ) iron(III)-superoxo complex bearing tetraamido macrocyclic ligand (TAML)<sup>19</sup>, [Fe<sup>III</sup>(TAML)(O<sub>2</sub>)]<sup>2-</sup> (**1**) (Fig. 1a; see also Supplementary Fig. 1 and Supplementary Table 1). The isolated iron(III)-superoxo complex undergoes both electrophilic and nucleophilic oxidation reactions. In addition, the iron(III)-superoxo complex transfers the bound O<sub>2</sub> unit to a manganese(III) analogue, resulting in the formation of a mononuclear side-on ( $\eta^2$ ) manganese(IV)-peroxo complex, [Mn<sup>IV</sup>(TAML)(O<sub>2</sub>)]<sup>2-</sup> (**2**) (Fig. 1b; see also Supplementary Fig. 2 and Supplementary Table 2). The electronic structures of **1** and **2** are investigated using density functional theory (DFT) calculations to elucidate the difference in the redox distribution between the metal ion and O<sub>2</sub> in these complexes.

## Results and discussion

### Synthesis and structural and spectroscopic characterization of iron(III)-superoxo complex

The reaction of  $\text{Na}[\text{Fe}^{\text{III}}(\text{TAML})]$  with solid potassium superoxide ( $\text{KO}_2$ ) in the presence of 6 equiv. of 2.2.2-cryptand in  $\text{CH}_3\text{CN}$  at  $5^\circ\text{C}$  immediately generated a red intermediate (**1**) with an electronic absorption band at  $\lambda_{\text{max}} = 490\text{ nm}$  ( $\epsilon = 2600\text{ M}^{-1}\text{ cm}^{-1}$ ) (Fig. 2a; Supplementary Experimental Section). The intermediate persisted for several days at  $-20^\circ\text{C}$ , and the greater thermal stability of **1** allowed us to isolate single crystals suitable for structural and spectroscopic analyses as well as for reactivity studies. The electrospray ionization mass spectrum (ESI MS) of **1** exhibits a prominent ion peak at a mass-to-charge ( $m/z$ ) ratio of 873.1, whose mass and isotope distribution pattern correspond to  $[\text{K}(2.2.2\text{-cryptand})\text{Fe}(\text{TAML})(\text{O}_2)]^-$  (calculated  $m/z$  of 873.3) (Fig. 2a, inset; also see Supplementary Fig. 3a). When the reaction was carried out with isotopically labeled  $\text{K}^{18}\text{O}_2$ , a mass peak corresponding to  $[\text{K}(2.2.2\text{-cryptand})\text{Fe}(\text{TAML})(^{18}\text{O}_2)]^-$  appeared at a  $m/z$  of 877.1 (calculated  $m/z$  of 877.3). The shift in four mass units on substitution of  $^{16}\text{O}$  with  $^{18}\text{O}$  indicates that **1** contains an  $\text{O}_2$  unit (Fig. 2a, inset). In the electron paramagnetic resonance (EPR) spectrum of a frozen acetonitrile solution of **1** recorded at 4.3 K, no signal was observed in both perpendicular and parallel modes (Supplementary Fig. 3b), which might arise from the electronic configuration of an iron(IV)-peroxo species ( $S = 1$  or  $2$ ) or an iron(III) species ( $S = 1/2, 3/2,$  or  $5/2$ ) coupled with an  $\text{O}_2^-$  unit of  $S = 1/2$ . The electronic configuration of **1** was further investigated with  $^1\text{H}$  NMR Evans method, and the magnetic moment of  $3.26\ \mu_{\text{B}}$  at  $-20^\circ\text{C}$  is consistent with an  $S = 1$  ground state for **1**. Based on those experimental results, there are three possible structures for **1**: (i) an Fe(IV)-peroxo species with  $S = 1$  Fe(IV), (ii) an Fe(III)-superoxo species with  $S = 1/2$  Fe(III) ferromagnetically coupled with  $S = 1/2$   $\text{O}_2^-$  moiety, or (iii) an Fe(III)-superoxo species with  $S = 3/2$  Fe(III) antiferromagnetically coupled with an  $S = 1/2$   $\text{O}_2^-$  moiety (vide infra). The infrared spectrum of **1**, collected in  $\text{CH}_3\text{CN}$  at  $-40^\circ\text{C}$ , exhibits an isotopically sensitive band at  $1260\text{ cm}^{-1}$ , which shifts to  $1183\text{ cm}^{-1}$  upon substitution of  $^{16}\text{O}$  with  $^{18}\text{O}$ , consistent with its assignment as an O-O stretching vibration on the basis of the  $^{16-18}$  value of  $77\text{ cm}^{-1}$  ( $^{16-18}$  (calculated) =  $72\text{ cm}^{-1}$ ) (Fig. 2b). This value is comparable to those recorded for metal-superoxo complexes<sup>9, 13, 20, 21</sup>, suggesting that the  $\text{O}_2$  unit in **1** possesses superoxo character.

Mössbauer spectroscopy was also performed to determine the oxidation state of iron in **1** and define its electronic structure (Fig. 2c,  $\delta = 0.10\text{ mm s}^{-1}$  and  $E_{\text{Q}} = 2.66\text{ mm s}^{-1}$ ). The isomer shift is in the same range as that for TAML complexes with  $S = 3/2$  Fe(III) centers<sup>22</sup>. Following the procedure of Chanda et al.<sup>22</sup>, the density at the nucleus  $\rho$  and  $E_{\text{Q}}$  for this complex were calculated using the 6-311G basis set and B3LYP functional (Supplementary Experimental Section); the density at the nucleus was converted into an isomer shift using the calibration of Vrajmasu et al.<sup>23</sup>. The computational isomer shift obtained using this method,  $\delta = 0.12\text{ mm s}^{-1}$ , and the calculated  $E_{\text{Q}}, 2.78\text{ mm s}^{-1}$ , are in excellent agreement with the experimental values. Thus, the spectroscopic data described above suggest that **1** is a mononuclear iron(III) species binding a superoxo ligand,  $\text{Fe}^{\text{III}}\text{-O}_2^-$ .

Direct evidence for an Fe–O<sub>2</sub> unit is unambiguously provided from the X-ray crystal structure of **1**, which revealed a mononuclear side-on 1:1 iron complex of O<sub>2</sub> with the triangular Fe–O<sub>2</sub> moiety having a small bite angle (40.37(9)° for O1-Fe1-O2, 39.9(2)° for O7-Fe2-O8, 39.4(4)° for O7'-Fe2-O8'), that results in a pseudo square pyramidal geometry with side-on biding O<sub>2</sub> moiety (Fig. 1a, also see Supplementary Fig. 1 and Supplementary Table 1). The crystallographically independent O–O bond lengths (O1-O2: 1.323(3) Å, O7-O8/O7'-O8' = 1.306(7)/1.315(12) Å) of **1** are significantly shorter than those of Fe(III)-peroxo species, such as [Fe<sup>III</sup>(TMC)(O<sub>2</sub>)]<sup>+</sup> (1.463(6) Å)<sup>10</sup> and naphthalene dioxygenase (ca. 1.45 Å)<sup>6</sup>, but similar to that of Fe(II)-superoxo species found in homoprotocatechuate 2,3-dioxygenase (1.34 Å)<sup>5</sup>. Further, the observed O–O bond length is close to those of other metal-superoxo complexes that have been characterized structurally (ca. 1.2–1.3 Å)<sup>9, 21</sup>. Furthermore, the O<sub>2</sub> ligand within Fe–O<sub>2</sub> unit is almost symmetrically bound to the iron ion with the average Fe–O bond length of 1.927 Å, which is slightly longer than that of [Fe<sup>III</sup>(TMC)(O<sub>2</sub>)]<sup>+</sup> (1.910 Å). In accordance with these experimental values, we conclude that **1** is an iron(III)-superoxo complex with the O<sub>2</sub> unit bound in a side-on fashion ( $\eta^2$ ). To the best of our knowledge, this is the first X-ray crystal structure of a mononuclear nonheme iron(III)-superoxo complex reported in nonheme iron enzyme and model systems.

### Reactivity studies of **1** in electrophilic and nucleophilic oxidation and O<sub>2</sub>-transfer

As presented in the Introduction, nonheme iron(III)-superoxo species have attracted much attention recently as active oxidants in a number of enzymatic reactions, especially in electrophilic oxidation reactions by isopenicillin *N* synthase, *myo*-inositol oxygenase, and cysteine dioxygenase<sup>2, 24, 25</sup>. However, nucleophilic reactivity of the nonheme iron(III)-superoxo species has not been previously reported. Moreover, reactivities of synthetic nonheme iron(III)-superoxo complexes in electrophilic and nucleophilic oxidation reactions have been rarely reported in biomimetic studies.<sup>20</sup> We therefore performed these reactions with the isolated, well-characterized nonheme iron(III)-superoxo complex, **1**. First, the reactivity of **1** was examined in the oxidation of C–H and O–H bonds, with precedents that metal-superoxo species are potent oxidants in the C–H and O–H substrate oxygenation reactions<sup>11, 26–28</sup>. Addition of substrates with weak C–H bonds, such as cyclohexadiene and xanthene, to **1** did not show any spectral changes, indicating that **1** is not capable of activating the C–H bonds of hydrocarbons. In the case of O–H bond activation, addition of 2,4-di-*tert*-butylphenol to **1** caused the decay of the intermediate with the concurrent formation of [Fe<sup>III</sup>(TAML)]<sup>−</sup> (Supplementary Fig. 4a). Clear isosbestic points were observed at 333 and 393 nm. The decay rate increased with increase of the substrate concentration, giving a second-order rate constant of  $3.0 \times 10^{-1} \text{ M}^{-1} \text{ s}^{-1}$  (Supplementary Fig. 4b). Product analysis of the reaction solution revealed the formation of 2,2'-dihydroxy-3,3', 5,5'-tetra-*tert*-butylbiphenol as a major product (~75% based on the intermediates used)<sup>29, 30</sup>. Further, reactions with *para*-substituted 2,6-di-*tert*-butylphenols (*p*-Y-2,6-*t*-Bu<sub>2</sub>-C<sub>6</sub>H<sub>2</sub>OH; Y = OMe, Me, H, CN) revealed that the electronegativity of the *para*-substituents significantly influences the reaction rates (Supplementary Fig. 5); a plot of the relative rates as a function of O–H bond dissociation energies (BDEs) of *p*-Y-2,6-*t*-Bu<sub>2</sub>-C<sub>6</sub>H<sub>2</sub>OH shows a good correlation with a slope of −0.65 (Supplementary Fig. 4c). In high-valent metal-oxo and metal-superoxo complexes, a linear relationship such as this has been cited in support of an H-atom abstraction mechanism in phenol O–H bond oxidations<sup>29–31</sup>.

The nucleophilic reactivity of **1** was investigated in aldehyde deformylation, using 2-phenylpropionaldehyde (2-PPA) as a substrate. Upon addition of 2-PPA to **1** in CH<sub>3</sub>CN at 5 °C, **1** was converted to the starting [Fe<sup>III</sup>(TAML)]<sup>-</sup> complex with a first-order decay profile (Supplementary Fig. 6a), and pseudo-first-order rate constants that increased proportionally with the aldehyde concentration ( $k_2 = 3.7 \text{ M}^{-1} \text{ s}^{-1}$ ) (Supplementary Fig. 6b). Product analysis of the resulting solutions revealed the formation of acetophenone (90% based on **1**), as frequently observed in other nucleophilic oxidation reactions by metal-peroxo complexes<sup>32, 33</sup>. The reactivity of **1** was further investigated using substituted benzaldehydes with a series of electron-donating and -withdrawing substituents at the *para*-position of the phenyl group (*para*-Y-Ph-CHO; Y = OMe, Me, H, Cl) (Supplementary Fig. 7). A positive  $\rho^+$  value of 1.4 in the Hammett plot was obtained (Supplementary Fig. 6c), demonstrating that the iron(III)-superoxo complex is an active nucleophilic oxidant; the nucleophilic reactivity of a copper(II)-superoxo complex was reported very recently<sup>34</sup>. To the best of our knowledge, the present results provide the first strong evidence for the involvement of iron(III)-superoxo species in nucleophilic oxidation reactions.

The reactivity of **1** was further investigated in an intermolecular O<sub>2</sub> transfer reaction (Fig. 3a), with precedents that metal-peroxo species {e.g., [Ni<sup>III</sup>(12-TMC)(O<sub>2</sub>)]<sup>+</sup>, [Co<sup>III</sup>(12-TMC)(O<sub>2</sub>)]<sup>+</sup>, and [Co<sup>III</sup>(13-TMC)(O<sub>2</sub>)]<sup>+</sup>} are capable of transferring their peroxo group to a manganese complex [Mn<sup>II</sup>(14-TMC)]<sup>2+</sup> to give a manganese-peroxo complex {e.g., [Mn<sup>III</sup>(14-TMC)(O<sub>2</sub>)]<sup>+</sup>}<sup>35, 36</sup>. Interestingly, addition of [Mn<sup>III</sup>(TAML)]<sup>-</sup> to a solution containing **1** immediately generated a blue intermediate (**2**) with an electronic absorption band at 600 nm (Fig. 3b); the blue intermediate **2** was characterized as a mononuclear side-on ( $\eta^2$ ) manganese(IV)-peroxo complex (vide infra). Clear isosbestic points were observed at 462 and 561 nm in the titration reaction (Fig. 3b; Supplementary Fig. 8), in which the O<sub>2</sub>-transfer from **1** to [Mn<sup>III</sup>(TAML)]<sup>-</sup> was found to have 1:1 reaction stoichiometry (Fig. 3b, inset). Kinetic studies of the O<sub>2</sub>-transfer from **1** to [Mn<sup>III</sup>(TAML)]<sup>-</sup> were performed in DMF at -20 °C under pseudo-first-order reaction conditions. Addition of 10 equiv. of [Mn<sup>III</sup>(TAML)]<sup>-</sup> to the solution of **1** yielded  $k_{\text{obs}}$  value of  $1.0 \times 10^{-2} \text{ s}^{-1}$  (Supplementary Fig. 9a), with the first-order rate constant increasing proportionally with the concentration of [Mn<sup>III</sup>(TAML)]<sup>-</sup> that gives a second-order rate constant ( $k_2$ ) of  $9.0 \times 10^{-1} \text{ M}^{-1} \text{ s}^{-1}$  at -20 °C (Supplementary Fig. 9b). The intermolecular O<sub>2</sub>-transfer reaction was dependent on temperature, from which a linear Eyring plot was obtained between -20 and 10 °C to give activation parameters of  $H^\ddagger = 55 \text{ kJ mol}^{-1}$  and  $S^\ddagger = -33 \text{ J mol}^{-1} \text{ K}^{-1}$  (Supplementary Fig. 10). The temperature dependence of the rate constants and the significant negative entropy value suggest that a bimolecular mechanism is operating in the O<sub>2</sub>-transfer reaction, where the formation of a presumed [(TAML)Fe-O<sub>2</sub>-Mn(TAML)]<sup>3-</sup> intermediate is the rate-determining step<sup>35, 36</sup>. Finally, the reverse reaction, which is the O<sub>2</sub>-transfer from **2** to [Fe<sup>III</sup>(TAML)]<sup>-</sup> to form [Mn<sup>III</sup>(TAML)]<sup>-</sup> and **1**, does not occur.

In this section, we have shown that the nonheme iron(III)-superoxo complex, **1**, is an active oxidant in both electrophilic and nucleophilic reactions. We have also shown that the O<sub>2</sub> unit in the iron(III)-superoxo complex is transferred to a Mn(III) complex. Detailed mechanistic studies are underway to understand the chemical properties and mechanisms of nonheme iron(III)-superoxo species in oxidation reactions.

## Synthesis and structural and spectroscopic characterization of manganese(IV)-peroxo complex

The manganese(IV)-peroxo complex,  $[\text{Mn}^{\text{IV}}(\text{TAML})(\text{O}_2)]^{2-}$  (**2**), was synthesized independently by reacting  $\text{Li}[\text{Mn}^{\text{III}}(\text{TAML})]$  with solid  $\text{KO}_2$  in the presence of 6 equiv. of 2.2.2-cryptand in  $\text{CH}_3\text{CN}$  at 25 °C (see Supplementary Fig. 11 and 12 and Supplementary Table 3 for the spectroscopic and structural characterization of  $[\text{Mn}^{\text{III}}(\text{TAML})]^-$ ). The high stability of **2** at room temperature allowed us to isolate single crystals suitable for structural and spectroscopic characterization. The UV-vis spectrum of **2** exhibits an absorption band at 600 nm ( $\epsilon = 720 \text{ M}^{-1} \text{ cm}^{-1}$ ) (Supplementary Fig. 13a). The ESI MS of **2** exhibits a prominent ion peak at a mass-to-charge ( $m/z$ ) ratio of 872.1, and its isotopic distribution pattern was in good agreement with  $[\text{K}(2.2.2\text{-cryptand})\text{Mn}(\text{TAML})(^{16}\text{O}_2)]^-$  (calculated  $m/z$  of 872.3) (Supplementary Fig. 13b). When **2** was prepared with isotopically labeled  $\text{K}^{18}\text{O}_2$ , a mass peak corresponding to  $[\text{K}(2.2.2\text{-cryptand})\text{Mn}(\text{TAML})(^{18}\text{O}_2)]^-$  appeared at a  $m/z$  of 876.1 (calculated  $m/z$  of 876.3). The shift in four mass units on substitution of  $^{16}\text{O}$  with  $^{18}\text{O}$  indicates that **2** contains an  $\text{O}_2$  unit (Supplementary Fig. 13b, inset). The EPR spectrum of **2** exhibits one six-line hyperfine pattern centered at  $g = 5.6$  with splitting of  $a = 55 \text{ G}$  and two broad signals at  $g = 2.3$  and 1.7, indicating an  $S = 3/2$  Mn(IV) ground state (Supplementary Fig. 13c)<sup>37, 38</sup>. The solid IR spectrum (KBr) of **2** exhibits an isotopically sensitive band at  $905 \text{ cm}^{-1}$ , which shifts to  $860 \text{ cm}^{-1}$  upon substitution of  $^{16}\text{O}$  with  $^{18}\text{O}_2$ , consistent with its assignment as an O-O stretching vibration on the basis of the  $^{16}\text{O}$ - $^{18}\text{O}$  value of  $45 \text{ cm}^{-1}$  ( $^{16}\text{O}$ - $^{18}\text{O}$  (calculated) =  $52 \text{ cm}^{-1}$ ) (Supplementary Fig. 14). This value is comparable to those recorded for metal-peroxo complexes<sup>38, 39</sup>, thus leading us to conclude that the  $\text{O}_2$  unit in **2** possesses peroxo character.

The X-ray crystal structure of **2** is given in Fig. 1b (also see Supplementary Fig. 2 and Supplementary Table 3). Although complex **2** also contains a mononuclear side-on 1:1 Mn- $\text{O}_2$  moiety best described a pseudo square pyramidal geometry with small acute angles of  $44.30(7)^\circ$  for O1-Mn1-O2,  $44.17(11)^\circ$  for O7-Mn2-O8, and  $43.9(4)^\circ$  for O7'-Mn2-O8' (Supplementary Fig. 2). By comparison with the structure of **1**, the O-O bond distances in **2** are significantly different. Contrary to the shorter O-O bond length of **1** determined by the X-ray crystal structure, the crystallographically independent O-O bond distances for **2** are 1.415(2) (O1-O2), 1.412(3) (O7-O8) and 1.403(13) (O7'-O8') Å, which are significantly longer than **1** and even longer than recently reported O-O bond distance of a mononuclear nonheme Mn(IV)-peroxo (1.379(3) Å) complex<sup>38</sup>. The average Mn-O distance of 1.876 Å is within the range of 1.841–1.901 Å for the monomeric side-on Mn(III)-peroxo complexes<sup>33</sup>. Moreover, this mean value is close to that of Mn(IV)-peroxo (1.878(2) Å) supported by tetradentate trianionic ligand<sup>38</sup>. Taken together, the spectroscopic and structural data unambiguously demonstrate that **2** is a high-spin ( $S = 3/2$ ) Mn(IV)-peroxo complex binding the  $\text{O}_2^{2-}$  unit in a side-on fashion ( $\eta^2$ ).

## Computational correlation of the geometric and electronic structures of Fe(III)-superoxo and Mn(IV)-peroxo complexes

In order to elucidate the electronic structures of **1** and **2**, DFT geometry optimizations were carried out on each complex starting from the atomic coordinates refined in both crystal structures and using its experimental spin state. For **1**, a series of functionals employing

varying amounts of Hartree-Fock exchange were used (BP86 [0%], TPSSh [10%], B3LYP [20%], BP86 + 25% HFX, and M06 [27%]), all with the TZVP basis set. The BP86 functional with 25% Hartree-Fock exchange gives an optimized structure most consistent with the crystallographic data (Supplementary Table 4 for geometric parameters). Note from Supplementary Table 4 that the O-O distance is most sensitive to functional and the experimental 1.32 Å distance, which reflects the amount of charge transfer from the metal to O<sub>2</sub>, is best reproduced by this hybrid functional (while M06 also gives a good O-O distance, its average Fe-O bond length is too long). For **2**, the geometry optimization results using the BP86, TPSSh, B3LYP, and M06 functionals were compared, and the closest agreement with the experimental O-O bond length was obtained using B3LYP (Supplementary Table 5). Since it was necessary to use a BP86 + 25% HFX to reproduce the structure of **1**, the Mössbauer parameters were recalculated using this functional (see Supplementary Fig. 15 for the calibration of experimental isomer shifts with calculated  $\rho$  at the Fe). The isomer shift obtained of  $\delta = 0.11 \text{ mm s}^{-1}$  is again consistent with the experimental value of  $0.10 \text{ mm s}^{-1}$ .

Since the DFT-derived geometry-optimized structures for **1** and **2** give reasonable agreement with the experimental data, their associated electronic structures were evaluated. The unoccupied orbitals calculated for **1** with significant Fe d or O<sub>2</sub>  $\pi^*$  character are displayed in Fig. 4a (the unoccupied orbitals reflect the uncompensated electron density in the occupied orbitals). From Fig. 4a, the electronic structure of **1** lies between the limits of an  $S = 1$  Fe(IV)-peroxo and an  $S = 3/2$  Fe(III) antiferromagnetically coupled to an  $S = 1/2$  superoxo species. The Mülliken population analysis of the unoccupied orbitals shows 78% O<sub>2</sub>  $\pi^*_\sigma$  character (where  $\pi^*_\sigma$  is the in-[Fe-O<sub>2</sub>]-plane  $\pi^*$  orbital on O<sub>2</sub>;  $\pi^*_\nu$  is out-of-plane) in the  $\alpha$ -unoccupied  $d_{xz}$  orbital and 15% O<sub>2</sub>  $\pi^*_\sigma$  character in the  $\beta$ -unoccupied  $d_{xz}$  orbital. From the Fe(IV)-peroxo limit, this is consistent with significant delocalization of an O<sub>2</sub><sup>2-</sup> electron onto the Fe and is thus closer to the Fe(III)-superoxo limit (Fig. 4b). The low energy unoccupied  $\pi^*_\sigma$  character on the superoxo is consistent with its H-atom abstraction reactivity. Similarly, for the calculated electronic structure of **2**, starting from the Mn(IV)-peroxo limit, the unoccupied orbitals (Supplementary Fig. 16) show delocalization of  $\alpha$  and  $\beta$  O<sub>2</sub><sup>2-</sup>  $\pi^*_\sigma$  electrons (47% and 21%, respectively) into the unoccupied Mn  $d_{xz}$  orbital, in addition to 10% delocalization of the  $\beta$  O<sub>2</sub><sup>2-</sup>  $\pi^*_\nu$  electron into the  $\beta$ -unoccupied  $d_{xy}$  orbital (which is occupied in **1**) (Fig. 4c). This gives a total delocalization of 78% of a O<sub>2</sub><sup>2-</sup>  $\pi^*$  electron onto the Mn, less than the delocalization onto Fe in **1** (93%), which places **2** closer to the Mn(IV)-peroxo limit, consistent with the longer O-O bond length in **2**.

To understand the differences between the geometric and electronic structures of **1** and **2**, an extra electron was added to each complex and the ionization energy of these hypothetical M(III)(TAML)-peroxo complexes was calculated, using the possible initial spin states ( $S = 3/2$  for Fe<sup>III</sup>,  $S = 1$  and 2 for Mn<sup>III</sup>) and the final spin states observed experimentally for **1** ( $S = 1$ ) and **2** ( $S = 3/2$ ). This evaluates whether there is a difference in the reduction potential between these metal ions in this ligand set. The results of these calculations are summarized in Supplementary Table 6, along with those of parallel calculations with a redox-innocent Cl<sup>-</sup> ligand in place of the peroxide. Relative to the iron complex, ionization of an electron from a hypothetical  $S = 1$  Mn(III)-O<sub>2</sub><sup>2-</sup> is easier by 0.42 eV (1.23 eV with the Cl<sup>-</sup> ligand),

while ionization of an electron from an  $S = 2$  Mn(III)-O<sub>2</sub><sup>2-</sup> is approximately isoenergetic. From Fig. 4c and Supplementary Fig. 16, the electronic structure of **2** has significant  $S = 1$  Mn(III) character. These calculations indicate that the reduction potential of the metal center in the MnO<sub>2</sub> complex is lower than that of the metal center in the FeO<sub>2</sub> complex, consistent with increased electron density donation from the peroxide in **1** that results in significant Fe(III)-superoxo character relative to **2**.

In summary, we have reported the first synthetic mononuclear nonheme iron(III)-superoxo complex and a manganese(IV)-peroxo complex bearing a common supporting ligand. The crystal structures of those intermediates determined via single crystal X-ray crystallography demonstrate unambiguously that the O<sub>2</sub> units in the iron(III)-superoxo and manganese(IV)-peroxo complexes are bound to the iron and manganese ions in a side-on fashion. The difference in electron distribution between the metal and the O<sub>2</sub> reflects the higher reduction potential of the Fe(III). The nonheme iron(III)-superoxo complex undergoes both electrophilic and nucleophilic oxidation reactions. This model study suggests that both reactivities might be important in nonheme iron enzymecatalysis, which remains to be evaluated.

## Methods

See experimental section in supplementary information for detailed experimental conditions and procedures, spectroscopic and kinetics analyses, and computational calculations.

## Supplementary Material

Refer to Web version on PubMed Central for supplementary material.

## Acknowledgments

The research was supported by NRF of Korea through the CRI (NRF-2012R1A3A2048842 to W.N.) and GRL (NRF-2010-00353 to W.N.) Programs. The publication was partially supported by National Institutes of Health (NIH) Grant Number 5 P41 RR001209 (E.I.S.).

## References

1. Kovaleva EG, Lipscomb JD. Versatility of biological non-heme Fe(II) centers in oxygen activation reactions. *Nature Chem. Biol.* 2008; 4:186–193. [PubMed: 18277980]
2. van der Donk WA, Krebs C, Bollinger JM Jr. Substrate activation by iron superoxo intermediates. *Curr. Opin. Struct. Biol.* 2010; 20:673–683. [PubMed: 20951572]
3. Solomon EI, et al. Copper active sites in biology. *Chem. Rev.* 2014; 114:3659–3853. [PubMed: 24588098]
4. Rivalta I, Brudvig GW, Batista VS. Oxomanganese complexes for natural and artificial photosynthesis. *Curr. Opin. Chem. Biol.* 2012; 16:11–18. [PubMed: 22481113]
5. Kovaleva EG, Lipscomb JD. Crystal structures of Fe<sup>2+</sup> dioxygenase superoxo, alkylperoxo, and bound product intermediates. *Science.* 2007; 316:453–457. [PubMed: 17446402]
6. Karlsson A, et al. Crystal structure of naphthalene dioxygenase: side-on binding of dioxygen to iron. *Science.* 2003; 299:1039–1042. [PubMed: 12586937]
7. Phillips SEV. Structure of oxymyoglobin. *Nature.* 1978; 273:247–248. [PubMed: 643089]



8. Collman JP, Gagne RR, Reed CA, Robinson WT, Rodley GA. Structure of an iron(II) dioxygen complex: a model for oxygen carrying hemeproteins. *Proc. Natl Acad. Sci. USA.* 1974; 71:1326–1329. [PubMed: 4524640]
9. Momenteau M, Reed CA. Synthetic heme dioxygen complexes. *Chem. Rev.* 1994; 94:659–698.
10. Cho J, et al. Structure and reactivity of a mononuclear non-haem iron(III)-peroxo complex. *Nature.* 2011; 478:502–505. [PubMed: 22031443]
11. Xing G, et al. Evidence for C-H cleavage by an iron-superoxide complex in the glycol cleavage reaction catalysed by *myo*-inositol oxygenase. *Proc. Natl Acad. Sci. USA.* 2006; 103:6130–6135. [PubMed: 16606846]
12. Mbughuni MM, et al. Trapping and spectroscopic characterization of an Fe<sup>III</sup>-superoxo intermediate from a nonheme mononuclear iron-containing enzyme. *Proc. Natl Acad. Sci. USA.* 2010; 107:16788–16793. [PubMed: 20837547]
13. Shan X, Que L Jr. Intermediates in the oxygenation of a nonheme diiron(II) complex, including the first evidence for a bound superoxo species. *Proc. Natl Acad. Sci. USA.* 2005; 102:5340–5345. [PubMed: 15802473]
14. Hong S, Lee Y-M, Shin W, Fukuzumi S, Nam W. Dioxygen activation by mononuclear nonheme iron(II) complexes generates iron-oxygen intermediates in the presence of an NADH analogue and proton. *J. Am. Chem. Soc.* 2009; 131:13910–13911. [PubMed: 19746912]
15. Badieli YM, Siegler MA, Goldberg DP. O<sub>2</sub> activation by bis(imino)pyridine iron(II)-thiolate complexes. *J. Am. Chem. Soc.* 2011; 133:1274–1277. [PubMed: 21207980]
16. Chen H, Cho K-B, Lai W, Nam W, Shaik S. Dioxygen Activation by a Non-Heme Iron(II) Complex: Theoretical Study toward Understanding Ferric-Superoxo Complexes. *J. Chem. Theory Comput.* 2012; 8:915–926. [PubMed: 26593354]
17. Mukherjee A, et al. Oxygen activation at mononuclear nonheme iron centers: a superoxo perspective. *Inorg. Chem.* 2010; 49:3618–3628. [PubMed: 20380464]
18. Lee Y-M, et al. Dioxygen activation by a non-heme iron(II) complex: formation of an iron(IV)-oxo complex via C-H activation by a putative iron(III)-superoxo species. *J. Am. Chem. Soc.* 2010; 132:10668–10670. [PubMed: 20681694]
19. Popescu D-L, et al. High-valent first-row transition-metal complexes of tetraamido (4N) and diamidodialkoxido or diamidophenolato (2N/2O) ligands: synthesis, structure, and magnetochemistry. *Coord. Chem. Rev.* 2008; 252:2050–2071.
20. Kundu S, et al. O-O bond formation mediated by a hexanuclear iron complex supported on a stannoxane core. *Chem. Eur. J.* 2012; 18:2787–2791. [PubMed: 22262528]
21. Cramer CJ, Tolman WB, Theopold KH, Rheingold AL. Variable character of O-O and M-O bonding in side-on ( $\eta^2$ ) 1:1 metal complexes of O<sub>2</sub>. *Proc. Natl Acad. Sci. USA.* 2003; 100:3635–3640. [PubMed: 12634422]
22. Chanda A, et al. (TAML)Fe<sup>IV</sup>=O complex in aqueous solution: synthesis and spectroscopic and computational characterization. *Inorg. Chem.* 2008; 47:3669–3678. [PubMed: 18380453]
23. Vrajmasu V, Münck E, Bominaar EL. Density functional study of the electric hyperfine interactions and the redox-structural correlations in the cofactor of nitrogenase. Analysis of general trends in <sup>57</sup>Fe isomer shifts. *Inorg. Chem.* 2003; 42:5974–5988. [PubMed: 12971768]
24. McCoy JG, et al. Structure and mechanism of mouse cysteine dioxygenases. *Proc. Natl Acad. Sci. USA.* 2006; 103:3084–3089. [PubMed: 16492780]
25. Brown CD, Neidig ML, Neibergall MB, Lipscomb JD, Solomon EI. VTVH-MCD and DFT studies of thiolate bonding to {FeNO}(7)/{FeO<sub>2</sub>}(8) complexes of isopenicillin N synthase: Substrate determination of oxidase versus oxygenase activity in nonheme Fe enzymes. *J. Am. Chem. Soc.* 2007; 129:7427–7438. [PubMed: 17506560]
26. Maiti D, et al. A 1:1 copper-dioxygen adduct is an end-on bound superoxo copper(II) complex which undergoes oxygenation reactions with phenols. *J. Am. Chem. Soc.* 2007; 129:264–265. [PubMed: 17212392]
27. Maiti D, et al. Reactions of a copper(II) superoxo complex lead to C-H and O-H substrate oxygenation: modeling copper-monoxygenase C-H hydroxylation. *Angew. Chem. Int. Ed.* 2008; 47:82–85.

28. Cho J, Woo J, Nam W. An “end-on” chromium(III)-superoxo complex: crystallographic and spectroscopic characterization and reactivity in C-H bond activation of hydrocarbons. *J. Am. Chem. Soc.* 2010; 132:5958–5959. [PubMed: 20392047]
29. Sastri CV, et al. Axial ligand tuning of a nonheme iron(IV)-oxo unit for hydrogen atom abstraction. *Proc. Natl Acad. Sci. USA.* 2007; 104:19181–19186. [PubMed: 18048327]
30. Yiu DTY, Lee MFW, Lam WWY, Lau T-C. Kinetics and mechanisms of the oxidation of phenols by a *trans*-dioxoruthenium(VI) complex. *Inorg. Chem.* 2003; 42:1225–1232. [PubMed: 12588160]
31. Cho J, et al. Chromium(V)-oxo and chromium(III)-superoxo complexes bearing a macrocyclic TMC ligand in hydrogen atom abstraction reactions. *Chem. Sci.* 2011; 2:2057–2062.
32. Wertz DL, Valentine JS. Nucleophilicity of iron-peroxo porphyrin complexes. *Struct. Bonding.* 2000; 97:37–60.
33. Cho J, Sarangi R, Nam W. Mononuclear metal-O<sub>2</sub> complexes bearing macrocyclic *N*-tetramethylated cyclam ligands. *Acc. Chem. Res.* 2012; 45:1321–1330. [PubMed: 22612523]
34. Pirovano P, et al. Nucleophilic reactivity of a copper(II)-superoxide complex. *Angew. Chem. Int. Ed.* 2014; 53:1–6.
35. Cho J, et al. Geometric and electronic structure and reactivity of a mononuclear ‘side-on’ nickel(III)-peroxo complex. *Nature Chem.* 2009; 1:568–572. [PubMed: 20711413]
36. Cho J, et al. Synthesis, structural, and spectroscopic characterization and reactivities of mononuclear cobalt(III)-peroxo complexes. *J. Am. Chem. Soc.* 2010; 132:16977–16986. [PubMed: 21062059]
37. Kim SH, et al. Reversible O-O bond cleavage and formation between Mn(IV)-peroxo and Mn(V)-oxo corroles. *J. Am. Chem. Soc.* 2010; 132:14030–14032. [PubMed: 20845972]
38. Lee C-M, et al. Structural and spectroscopic characterization of a monomeric side-on manganese(IV) peroxo complex. *Angew. Chem. Int. Ed.* 2012; 51:1–5.
39. Shook RL, et al. A monomeric Mn<sup>III</sup>-peroxo complex derived directly from dioxygen. *J. Am. Chem. Soc.* 2008; 130:8888–8889. [PubMed: 18570414]

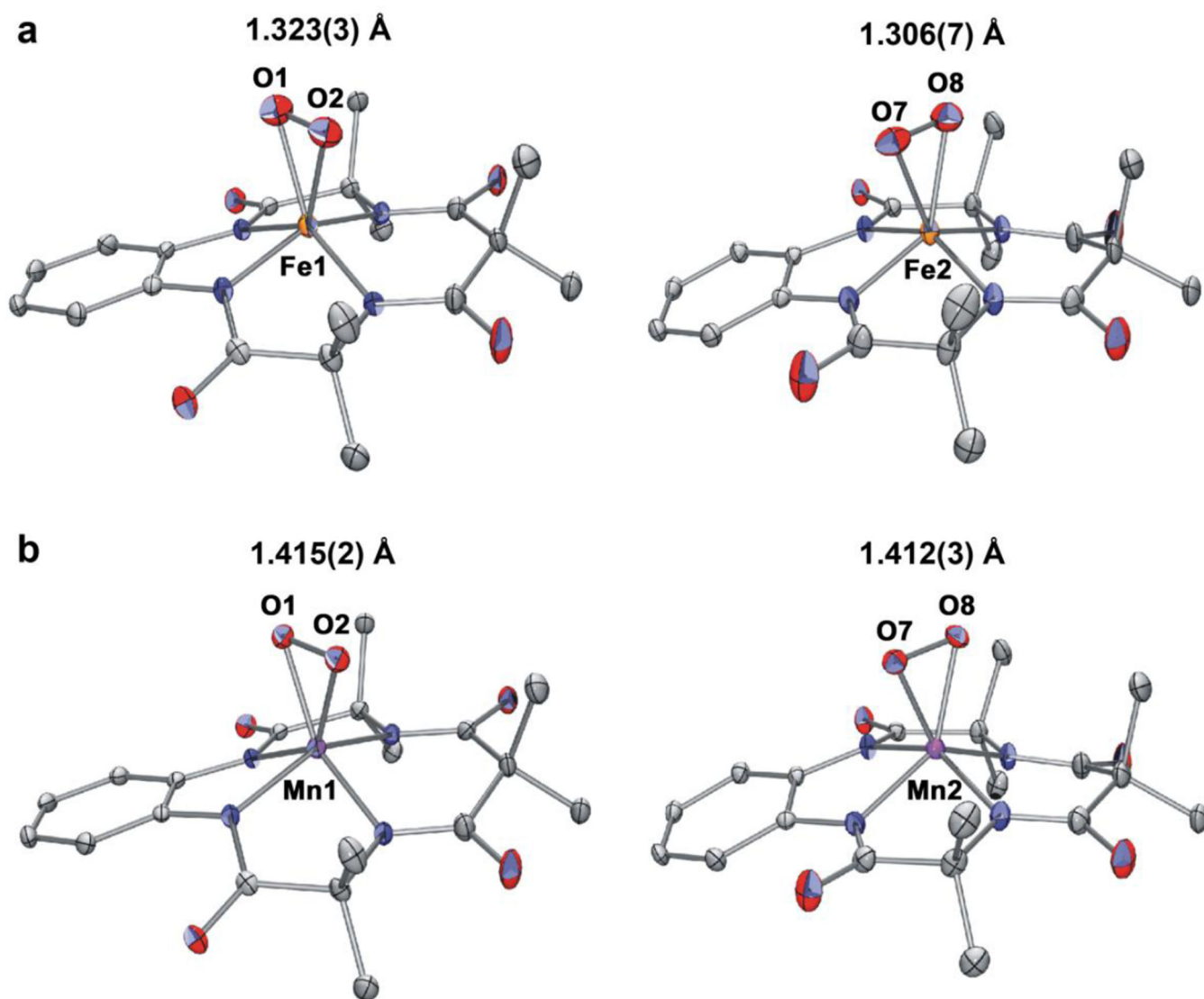


**Figure 1. X-ray crystal structures of 1 and 2**

**a**, Displacement ellipsoid plots (30% probability level) of the two crystallographically independent moieties of  $[\text{Fe}^{\text{III}}(\text{TAML})(\text{O}_2)]^{2-}$  in  $[\text{K}(2.2.2\text{-cryptand})(\text{CH}_3\text{CN})][\text{K}(2.2.2\text{-cryptand})]_3\text{-}[\text{Fe}^{\text{III}}(\text{TAML})(\text{O}_2)]_2$  (see also Supplementary Fig. 1 and Supplementary Tables 1). The O-O bond distances for the two independent moieties are 1.323(3) Å and 1.306(7) Å, respectively. Disorder of the O7-O8 and the H atoms have been omitted for the sake of clarity. **b**, Displacement ellipsoid plots (30% probability level) of the two crystallographically independent moieties of  $[\text{Mn}^{\text{IV}}(\text{TAML})(\text{O}_2)]^{2-}$  in  $[\text{K}(2.2.2\text{-cryptand})(\text{CH}_3\text{CN})][\text{K}(2.2.2\text{-cryptand})]_3\text{-}[\text{Mn}^{\text{IV}}(\text{TAML})(\text{O}_2)]_2$  (see also Supplementary Fig. 2 and Supplementary Tables 2). The O-O bond distances for the two independent moieties are 1.415(2) Å and 1.412(3) Å, respectively. Disorder of the O7-O8 and the H atoms have been omitted for the sake of clarity.

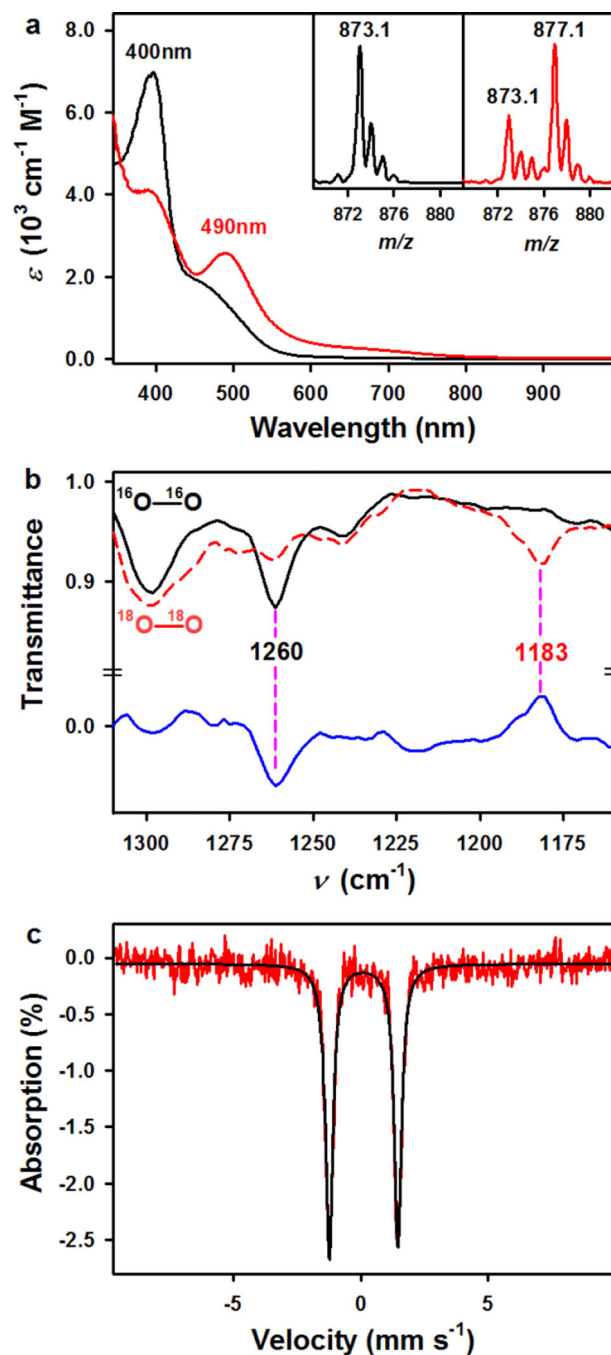


**Figure 2. Characterization of 1**

**a**, UV-vis spectra of  $[\text{Fe}^{\text{III}}(\text{TAML})]^-$  (black line, 0.25 mM) and  $[\text{Fe}^{\text{III}}(\text{TAML})(\text{O}_2)]^{2-}$  (**1**, red line, 0.25 mM) in  $\text{CH}_3\text{CN}$  at 5 °C. Insets show negative mode ESI MS spectra of  $[\text{Fe}^{\text{III}}(\text{TAML})(^{16}\text{O}_2)]^{2-}$  (**1- $^{16}\text{O}_2$** ) (left panel) and  $[\text{Fe}^{\text{III}}(\text{TAML})(^{18}\text{O}_2)]^{2-}$  (**1- $^{18}\text{O}_2$** ) (right panel) obtained in  $\text{CH}_3\text{CN}$  at -20 °C (see also Supplementary Fig. 3b for a full range of spectrum). **b**, Solution IR spectra of **1- $^{16}\text{O}_2$**  (black line, 2.0 mM) and **1- $^{18}\text{O}_2$**  (red line, 2.0 mM) in  $\text{CH}_3\text{CN}$  at -40 °C. Blue line is a difference spectrum of **1- $^{18}\text{O}_2$**  and **1- $^{16}\text{O}_2$** . **c**,

Mössbauer spectrum of **1** at 4.2K in the absence of field.  $\delta = 0.096 \text{ mm s}^{-1}$ ,  $E_q = 2.696 \text{ mm s}^{-1}$ , consistent with an intermediate-spin Fe(III) center bound to a TAML ligand.

Author Manuscript

Author Manuscript

Author Manuscript

Author Manuscript

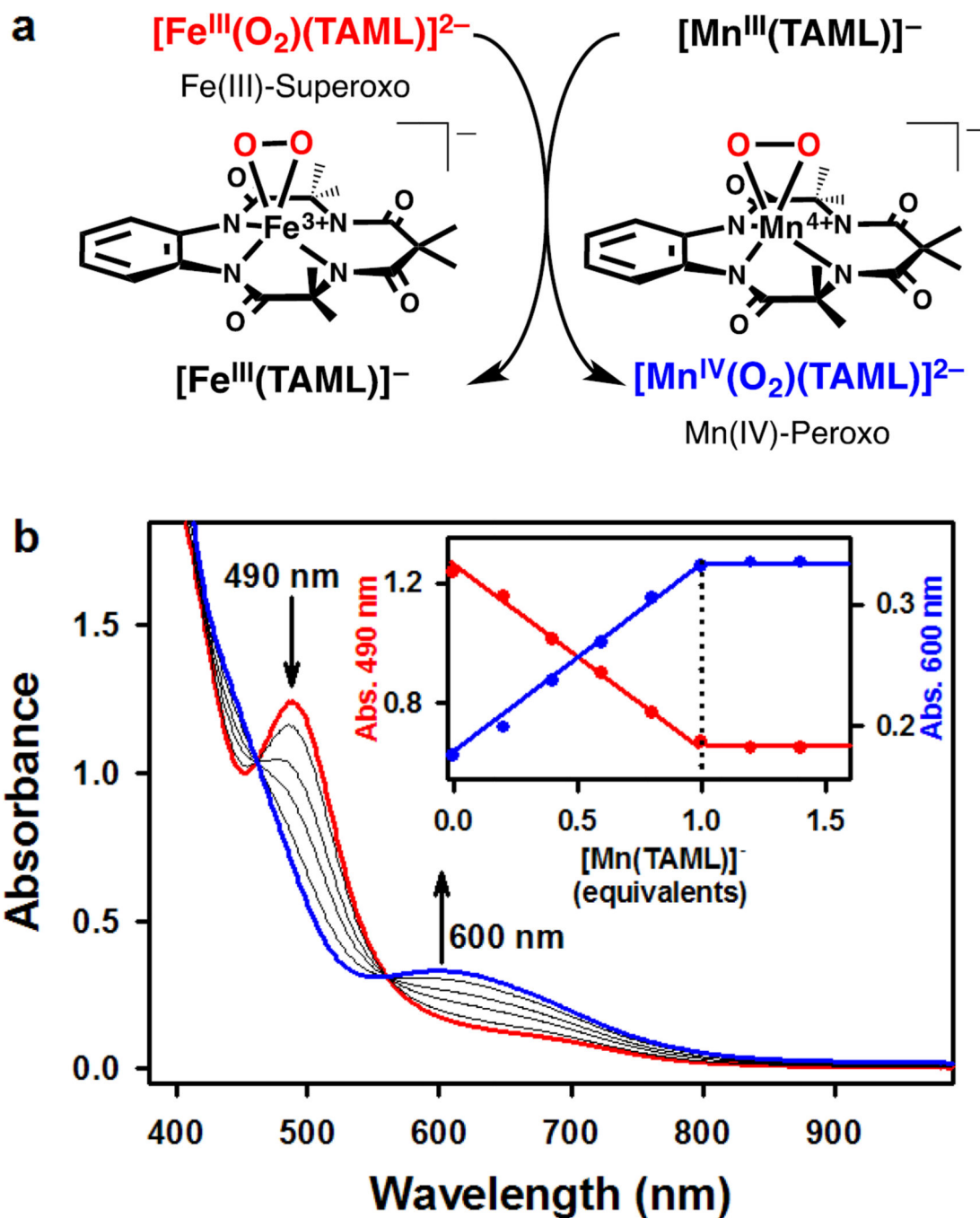


**Figure 3.** O<sub>2</sub>-transfer reaction of **1**

**a**, A reaction scheme showing O<sub>2</sub>-transfer from  $[\text{Fe}^{\text{III}}(\text{TAML})(\text{O}_2)]^{2-}$  (**1**) to  $[\text{Mn}^{\text{III}}(\text{TAML})]^{-}$  that results in the formation of  $[\text{Fe}^{\text{III}}(\text{TAML})]^{-}$  and  $[\text{Mn}^{\text{IV}}(\text{TAML})(\text{O}_2)]^{2-}$  (**2**). **b**, UV-vis spectral changes showing the formation of **2** (blue line) and the disappearance of **1** (red line) upon addition of  $[\text{Mn}^{\text{III}}(\text{TAML})]^{-}$  to **1** in increments of 0.2 equiv. in DMF at  $-20\text{ }^{\circ}\text{C}$ . Inset shows the spectroscopic titration at 490 nm (red circle) for the decay of **1** and 600 nm (blue circle) for the formation of **2** as a function of the equivalents of  $[\text{Mn}^{\text{III}}(\text{TAML})]^{-}$  added to **1**.

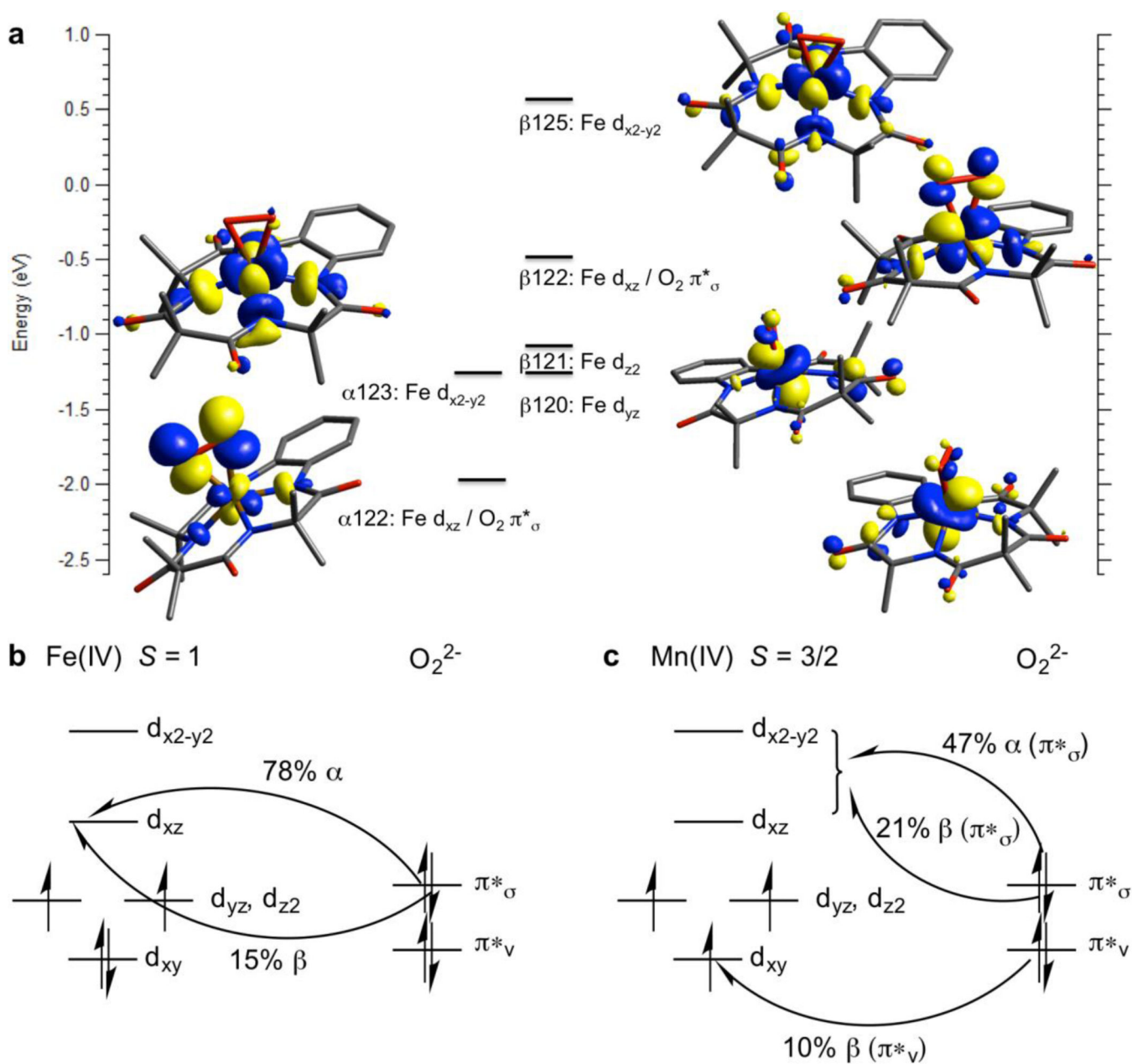


**Figure 4. DFT calculations on 1 and electronic structures for 1 and 2**

**a**, Unoccupied MOs for **1** with significant Fe or  $O_2 \pi^*$  character. **b**, Derived from the MOs presented in **a**, which show 78% delocalization of the  $\alpha \pi^*_{\sigma}$  electron and 15% delocalization of the  $\beta \pi^*_{\sigma}$  electron from  $O_2$  into the unoccupied Fe  $d_{xz}$  orbital, leading to significant  $S = 3/2$  Fe(III) antiferromagnetically coupled to  $S = 1/2$   $O_2$  character. **c**, Derived from the MOs presented in Supplementary Fig. 16.